Impact of contour scanning and helium-rich process gas on performances of Alloy 718 lattices produced by laser powder bed fusion

Materials & Design 215 (2022) 110501

Contents lists available at ScienceDirect

Materials & Design

journal homepage: www.elsevier.com/locate/matdes

Impact of contour scanning and helium-rich process gas on performances of Alloy 718 lattices produced by laser powder bed fusion

C. Pauzon [a,*], T. Mishurova [b], M. Fischer [c], J. Ahlström [a], T. Fritsch [b], G. Bruno [b,d], E. Hryha [a]

[a] Chalmers University of Technology, Industrial and Materials Science, Göteborg, Sweden
[b] Bundesanstalt für Materialforschung und–prüfung (BAM), Germany
[c] 3D Medlab, Marignane, France
[d] Institute of Physics and Astronomy, University of Potsdam, Potsdam, Germany

HIGHLIGHTS

- Less spatters were detected during printing Alloy 718 without contour scanning and with additions of He to the Ar gas.
- The microstructure, dimensional accuracy and behaviour under compression were unaffected by the process gas type.
- Promising results for process stability and to limit powder bed degradation, enhance powder reusability and the process sustainability.
- With contour scanning, dimensional accuracy and compression strength are maximized.
- Alloy 718 gyroid lattices produced by laser powder bed fusion exhibit a remarkably smooth and continuous hardening behaviour.

GRAPHICAL ABSTRACT

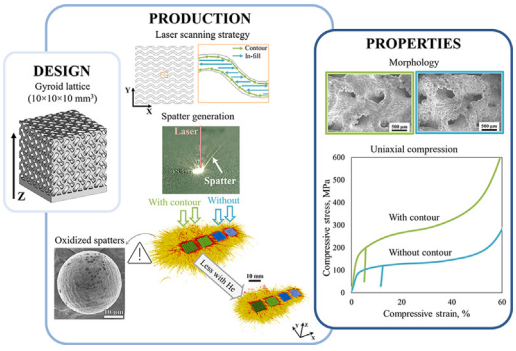

ARTICLE INFO

Article history:
Received 22 November 2021
Revised 14 February 2022
Accepted 27 February 2022
Available online 7 March 2022

Keywords:
Additive manufacturing
Laser powder bed fusion
Gyroid lattice
Process atmosphere
Alloy 718
Spatters

ABSTRACT

Contour scanning and process gas type are process parameters typically considered achieving second order effects compared to first order factors such as laser power and scanning speed. The present work highlights that contour scanning is crucial to ensure geometrical accuracy and thereby the high performance under uniaxial compression of complex Alloy 718 lattice structures. Studies of X-ray computed tomography visualizations of as-built and compression-strained structures reveal the continuous and smooth bending and compression of the walls, and the earlier onset of internal contact appearance in the denser lattices printed with contour. In contrast, the effect of addition of He to the Ar process gas appears to have limited influence on the mechanical response of the lattices and their microstructure as characterized by electron backscattered diffraction. However, the addition of He proved to significantly enhance the cooling rate and to reduce the amount of the generated spatters as evidenced by in situ monitoring of the process emissions, which is very promising for the process stability and powder reusability during laser powder bed fusion.

* Corresponding author.
E-mail address: camille.pauzon@simap.grenoble-inp.fr (C. Pauzon).

https://doi.org/10.1016/j.matdes.2022.110501
0264-1275/

1. Introduction

Metal laser powder bed fusion (LPBF) allows to produce complex geometry components by selectively melting a bed of micron-sized powder in a layer-wise approach. This process is also designated as laser-based powder bed fusion of metals (or PBF-LB/M) by the international standard ISO/ASTM 52900:2021 [1]. This manufacturing route permits to reconsider and revise designs to benefit from the possible integration of different functions, such as load bearing and heat transfer, while optimizing material utilisation to ensure lightweight structures. This approach is applied to develop cellular materials or lattice structures with unique properties, among which high specific strength, energy absorption, thermal and acoustic properties can be optimised [2]. More particularly, 316L stainless steel gyroid lattice structures have been identified as exhibiting globally increasing strain hardening and desirable energy absorption performance [3,4]. As underlined by Yan et al. [5], the gyroid lattice is characterised by smooth struts and a round core, offering a continuous variation of inclination angle of surfaces of the cell, without abrupt changes typical for structures with beam-like struts. This confers the gyroid structure with self-supporting properties particularly suitable for printing without support structures.

Special interest lies in the combination of the Alloy 718 material properties and the gyroid lattice design. Alloy 718 is a superalloy developed since the early 1950s for jet engine applications and recently designed aeroplanes still depend on this alloy [6]. It is a nickel–iron based alloy characterized by high mechanical strength and corrosion resistance at operating properties close to 650 °C [6]. These properties have also made it an interesting material for the oil and gas industry in applications such as valves, cryogenic storage tanks and heat exchangers. As emphasized by Parbat et al. [7], the lattice design can further improve the properties of heat exchangers by enhanced mixing and convection utilizing the extended surface area.

Despite the freedom of design granted by LPBF, deviations of produced geometries from the initial CAD file at the sub-millimetre scale stem from the difficulty to control the melt pool stability and optimize the process parameters [8]. Indeed, several studies report that the thickness, shape and connection of the lattice elements depends on the melt pool size [9,10]. First order parameters are typically considered to include the laser power, scanning speed, hatch distance and layer thickness. Still, the investigations by Artzt et al. [11] reveals that variables such as scanning strategy and contour parameters can have a major influence on the surface roughness and residual stress of simple cuboids and therefore geometry accuracy. Typically, a trade-off between optimised process parameters, for high density and mechanical properties, and reduced build rate is desirable for the further adoption of LPBF [12]. It is therefore paramount to evaluate the impact of contour scanning on structures with extensive amount of surfaces such as lattices, both in terms of performance and productivity.

Besides the above-mentioned parameters, the LPBF process atmosphere has also been identified as a factor influencing melt pool stability. Processing Ti-6Al-4V under pure He instead of the traditionally employed Ar permitted to significantly stabilize the melt pool as reflected by the reduced generation of visible incandescent spatters [13]. Similar results were obtained by Traore et al. [14] for Inconel® 625. More recent results [15] put in evidence that intermediate mixtures of He with Ar still offer the same benefits. These hot spatters are process by-products – metal ejections – from or produced close to the melt pool, driven by vaporization and Marangoni effects. Their generation is associated with reduced and inhomogeneous laser energy input to the material and leads to quality loss of the manufactured component. In addition, recent work highlighted that the production of Alloy 718 lattice structure compared to bulk material tends to promote powder bed degradation [16]. The manufacturing of a capsule with integrated dense body-centered tetragonal lattice was associated with a slight oxygen pick-up of the surrounding powder bed (~5% compared to fresh powder) analysed by combustion analysis. This finding was consistent with a small increase of the normalised oxygen content close to the particles surface measured by means of X-ray photoelectron spectroscopy. The authors connected this degradation to concentration of spatters in the powder bed surrounding the lattice structures. In light of these results, He addition to the traditional Ar should be further investigated as to their effect on lattice geometry accuracy and spatter generation.

The present study provides new insights on the relationship between process parameters, including the influence of contour scanning and the addition of He to Ar as process gas, the LPBF process stability and the produced Alloy 718 gyroid lattice geometry and mechanical performance. Alloy 718 gyroid lattices were manufactured with the in situ monitoring of the spatter generation, and were further evaluated by X-ray computed tomography, high resolution scanning electron microscopy and under uniaxial compression testing.

2. Experimental method

2.1. Lattice production

The Alloy 718 lattice structures studied in this work have been produced on an EOS M290 machine (EOS GmbH) equipped with an Yb-fibre laser of 400 W nominal power, a laser spot diameter of approximately 100 μm and a total build envelope of $250 \times 250 \times 325$ mm^3. The design of the built lattices is presented in Fig. 1 and consists of a gyroid structure, first described by Schoen in 1970 [17], which belongs to the family of triply periodic minimal surfaces (TPMS). Minimal surfaces have a zero mean curvature and TPMS are such that they repeat themselves in three dimensions and form a lattice. The gyroid lattices examined in this study fill a volume of $10 \times 10 \times 10$ mm^3, and the nominal CAD geometry has a relative density of approximately 0.41. The distribution of nominal wall thickness of the lattice is presented in the results section and compared to that of the printed lattices as measured by X-ray computed tomography, see Fig. 6. Lattices based on this design were produced using a 40 μm layer thickness, on top of 3 mm high dense support structures. Two sets of laser parameters were used to print the lattices i.e., with and without contour scanning, presented in more detail below.

The gas atomised virgin Alloy 718 powder used as feedstock was supplied by Höganäs AB, Sweden. Its particle size distribution as measured by laser diffraction using a Mastersizer 3000 (Malvern Panalytical) was as follows: D_{10} = 17.8 ± 0.1 μm, D_{50} = 30.1 ± 0.1 μm, D_{90} = 49.5 ± 0.2 μm.

Fig. 2 displays the layout of the build job conducted, where the colour of the lattices is specific to the laser parameters used. For five positions on the baseplate, two lattices per parameter set were printed. The first set of parameters is under the license *IN718_PerformanceM291 2.11*. It is a tailored combination of laser parameters (scanning speed, power, hatching distance, etc.) and features an *infill* scanning sequence (to scan the interior of the area to be scanned), *up*- and *down-skin* scannings for the upward and downward facing surfaces, as well as *contour* scanning where the laser draws the contour of the scanned area. The *in-fill* scanning follows a stripe scanning strategy with a rotation of 67° of the scan vectors between layers. The *contour* scanning is characterized by a slightly reduced linear energy input compared to the *in-fill*. The second set of parameters used is based on the first set, but the contour scan-

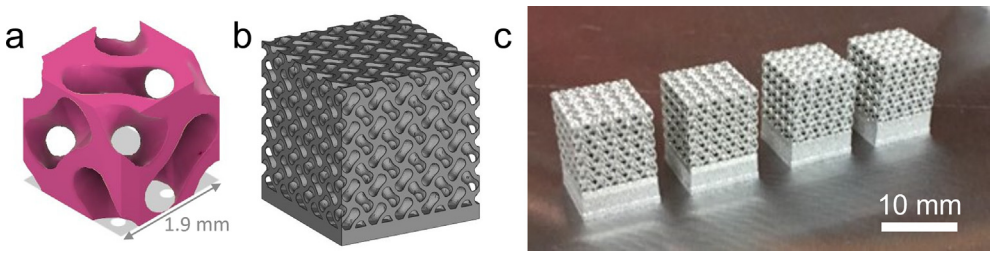

Fig. 1. CAD design of (a) the unit cell and (b) the lattice structure, including a 1 mm thick support; (b) photograph of produced lattices, with a total thickness of bulk support of 3 mm.

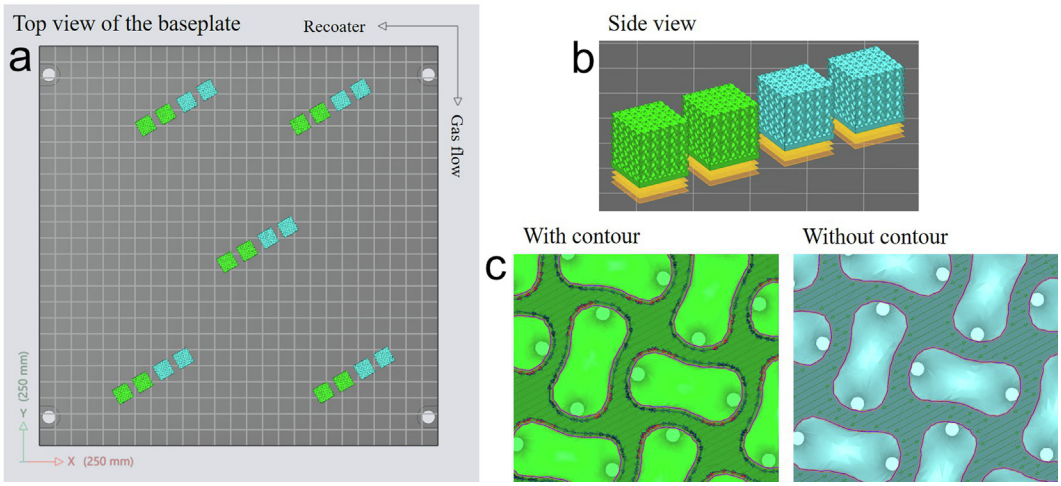

Fig. 2. Layout of the build job on the baseplate of the EOS M290: (a) Top view, (b) Side view on row of lattices, (c) Close-up on the cross-section of the lattices in the XY plane depicting the laser scan vectors. The green lattices are built with contour scanning and the blue ones without. (For interpretation of the references to colour in this figure legend, the reader is referred to the web version of this article.)

ning is removed. The inserts in Fig. 2 show in more detail the path of the laser for the two sets. Additionally, dense cubes of dimensions $10 \times 10 \times 10$ mm^3 produced with the same laser parameters were used as reference for porosity and microstructures.

The described build job was conducted under both the standard Ar atmosphere and a mixture of Ar and He referred to in this work as ADDvance® Laser230, see properties in Table 1. Both gases are of high quality with less than 40 ppm impurities. As described elsewhere [18], the LPBF process atmosphere is established by flushing the process chamber with the shielding gas until the residual oxygen is detected to be equal or less than 1000 ppm (or 0.1%). This is followed by a recirculation of this gas thanks to a pump that establishes a constant gas flow over the baseplate of approx. 2.2 m/s.

2.2. Process monitoring

The LPBF machine EOS M290 was equipped with the optical tomography monitoring system (EOSTATE Exposure OT) also provided by the machine manufacturer. It was used during this work to study the generation of spatters during the process. The system uses an off-axis 5-megapixel high-speed scientific complementary metal-oxide semiconductor (sCMOS) camera at the top of the build chamber observing the full powder bed, so that each pixel corresponds to a specific position on the layer, with a resolution of 125 μm per pixel. A geometric correction is applied to the images by the machine software to compensate for the non-central position of the camera. A bandpass filter passing signals with wavelength 900 ± 12.5 nm is placed on the camera, so that contribution from backscatter laser radiation (1064 nm), thermal radiation in the visible light (~380–780 nm) and plasma radiation from evaporation and ionization of gases (400–600 nm) are cut [20]. As one layer is scanned by the laser, digital images are collected with a 10 Hz frequency, and combined into a single output image per layer. In this work, each pixel of this single output image represents the maximum intensity at its corresponding position on the exposed layer during the complete laser scanning. The value of a pixel is connected to photon emission at the corresponding position during the laser scanning of the powder layer. With this setup only the emissions in the near-IR range contribute to the greyscale image. The contribution to each pixel can be caused by the thermal

Table 1
List of gas properties at atmospheric pressure relevant to this study (from Linde's internal data).

Gas	Density (kg/m^3)	Specific heat capacity at constant pressure (J/(kg·K))	Volumetric heat capacity (J/(m^3·K))	Thermal conductivity at 25 °C (W/(m·K))
Ar	1.62	520	842	0.016
ADDvance® Laser230	1.18	734	866	0.035
He	0.16	5190	830	0.142

radiation when the laser melts and/or heats the position corresponding to this pixel, or by the radiation from hot objects at that same position such as flying hot spatters.

All the images collected for each build job were further analysed in terms of spatter intensity and 3D spatial repartition with the software Dragonfly (Dragonfly 2020.1, Object Research Systems (ORS) Inc, Montreal, Canada, 2020) and in terms of spatter density, i.e. amount of spatter reaching each pixel, with the public domain ImageJ shareware [19]. For the 3D analysis, multiple image segmentation operations were applied to extract the volumes of the parts and of the spatters with a distinction based on intensity with three levels of brightness. While considering the brightest pixel in the image stack to have a 100% intensity, the "high intensity" spatters are between 1.5% and 13% of intensity (represented in red in the result images), the "medium intensity" spatters are between 1.2% and 1.5% intensity (orange) and the "low intensity" spatters are between 0.9% and 1.2% intensity (yellow).

For the 2D analysis of spatter density, the methodology is fully detailed in a dedicated publication [20]. In brief, firstly the pixels values corresponding to the scanned areas with the largest contribution from melt pool radiation were cropped away to only consider the outside pixels and study emissions from outside the parts corresponding to spatters. Similarly, images corresponding to the support of the lattice were removed to only consider lattice scanning emissions. Then, a threshold was applied to identify the spatter in the images from all the layers, and the corresponding pixels were attributed a value of 1. The images from the entire build are added together so that the grey level of each pixel represents the amount of spatter having reached that pixel. In the final image, the darker pixels correspond to the highest amounts of spatter. In other words, if a pixel is black, a spatter has reached the pixel in 100% of the layers while if a pixel is white, a spatter has reached it in 0% of the layers. Finally, isolines of equal pixel amounts are drawn to help the interpretation of results.

2.3. Compression testing

Quasi-static uniaxial compression testing of the lattice structures was performed at room temperature following requirements described in ISO 13314:2011[21]. An Instron 5500R electromechanic machine equipped with a 100 kN load-cell was used for the tests, and the LVDT displacement sensor was used for strain measurement. Before testing the lattices, the machine compliance was determined and used to compensate the displacement measurement by subtracting the machine deflection as a function of applied force. This is required to correctly compute the strain in the lattices.

The tests are performed at a constant crosshead speed of 0.01 mm/s, to achieve an initial compression strain rate of about 10^{-3} s^{-1}. For each lattice type and process gas, a preliminary test was performed to estimate the plateau stress, to determine the start and reversal point of the hysteresis loop for the following tests. This hysteresis loop permits to determine the elastic gradient (analogous to the Young's modulus of bulk materials) of the structures. From the recorded preliminary tests, the hysteresis loop for the lattices produced with contour scanning was performed between 20 kN and 5 kN, and for the lattices without contour between 12 kN and 3 kN. The compression continues after the hysteresis cycle up to a force of 90 kN.

From the recorded data, the following results were extracted: the plateau stress taken between 20% and 30% strain, the plateau end stress defined as 1.3 times the plateau stress, the corresponding plateau end strain, the quasi-elastic and the elastic gradients.

Additional compression tests were performed to compare the spring-back of the two kinds of structure at intermediate remaining strain levels of approximately 16% and 35%, by recording the unloading part of the curve. These specimens were also examined using X-ray computed tomography (see below) to characterise the shape of the deformed geometries and to identify possible internal contacts.

2.4. X-ray computed tomography

For each process gas and parameter set, one as-built lattice underwent laboratory X-ray computed tomography (XCT) to determine dimensional accuracy. Also two pre-strained structures (to 16% and 35%) were scanned to observe the deformation. XCT scan was performed using a Sauervein system, working with a X-ray tube voltage of 90 kV and a current of 210 mA and a voxel size of 12 μm. The thin foils of 0.25 mm of Cu and 0.25 mm of Ag were used as physical filters of the X-ray beam. VG Studio Max 3.1 software package was used for visualization, nominal-actual comparison (NAC) with the lattice CAD design and the wall thickness analysis using the sphere method.

2.5. Microscopy

High resolution scanning electron microscopy (HR SEM) using a LEO Gemini 1550 was conducted to image the surface morphology of the produced lattices. Prior to that, the lattices were ultrasonically cleaned in ethanol and dried in a vacuum chamber. The lattices were mounted in resin to observe their cross-section along the building direction (Z) and perpendicular to it (XY). The samples were prepared following the recommendations from Struers until achieving mirror finish and a last polishing step with OP-S suspension [22]. The polished cross-sections were observed using a light optical microscope (LOM) ZEISS Axioscope 7. The software ImageJ was used to measure the internal porosity on these polished cross-sections.

Electron backscattered diffraction (EBSD) was finally conducted using the HR SEM equipped with a Nordlys II detector (Oxford Instruments) and the HKL Channel 5 processing software to determine grain boundaries and orientations. An acceleration voltage of 20 kV was used with a step size of 1.5 μm. Minor noise reduction was applied on the recorded orientation maps, i.e. wild spikes removal and minor noise reduction (7 nearest neighbours required). The high angle grain boundaries were defined by a misorientation greater than 10°.

3. Results

3.1. Spatter generation

The quantity of collected spatters under Ar and the Ar-He mixture were rather similar, with about 0.1 g deposited on the gas inlet and 0.4 g inside of the gas outlet. Fig. 3 shows the images obtained from the post-processing of the EOSTATE Exposure OT data. Fig. 3 (a, b) displays all the detected spatters for a given row which is representative of all (similar results in all groups). Three colours are used and correspond to high (red), medium (orange) and low (yellow) intensity spatters as explained in 2.2. Spatters describe segments from the part edges to the outside. Each segment corresponds to the trajectory of a spatter which temperature is high enough to emit radiation in the near-IR wavelengths. The high intensity – hotter – spatters, concentrated close to the lattice edges, appear in higher amount with Ar compared to Ar-He. Regardless of the detected intensity, the spatter trajectories are significantly shorter with the addition of He to the process gas, which is associated to higher cooling rates of spatters. In addition, according to the lattice placements displayed in Fig. 2, it is clear

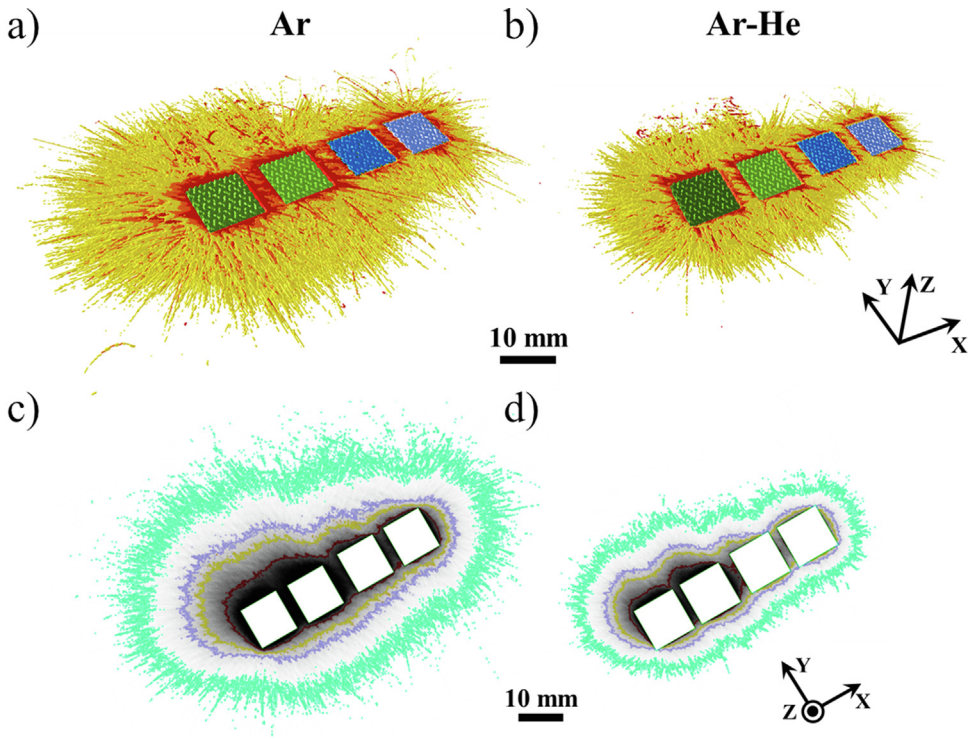

Fig. 3. Data collected with the monitoring system for a row of two lattices with contour (left) and two lattices without contour (right). (a-b) Reconstructed 3D image of all the detected spatters in Ar and Ar-He (yellow corresponds to low intensity spatters, orange to medium intensity pixels, red to high intensity pixels), (c-d) Images depicting spatter density, obtained by the addition of the all layer images (after binarization) for Ar and the Ar-He mixture. Isolines corresponding to 46% (green), 15% (purple), 3% (yellow) and 0.4% (red) of layers having a spatter at the concerned pixel location, are displayed for better visualisation. (For interpretation of the references to colour in this figure legend, the reader is referred to the web version of this article.)

that spatters are reduced when no contour scan is applied, in other words with reduced scanned length per part.

The proposed method to analyse this EOSTATE Exposure OT data permits to observe the density of generated spatters with intensities above a threshold which is kept constant for both gases. The resulting image has values depending on how many spatters (above the threshold) have reached that pixel (position on the baseplate). Therefore, the density as described herein is not strictly disconnected from the length of spatter trajectory and thus cooling rate. Still, as the isolines are more distanced from the lattices' edges in Ar compared to Ar-He, it is clear that both the amount of spatter is higher and that their cooling rate is lower in Ar compared to Ar-He.

3.2. Surface morphology and dimensional accuracy

Fig. 4 depicts the morphology of the front side of the lattice structures produced under Ar with and without contour scanning. As suggested by the reconstructed XCT slices along the building direction ("BD" in Fig. 5), the surfaces of the lattices built without contour scanning appear rougher with more sintered particles and apparent lack of bonding, independent on the gas atmosphere. The up-skin layers are smoother than the down-skin where the partially molten powder particles are attached. This is valid for all types of lattice samples (Fig. 5).

Fig. 6a shows the deviation of the actual lattice dimensions from the CAD design. Lattice structures with contour show the maximum deviation around zero values, showing high manufacturing accuracy. In contrast, the samples without contour have the maximum deviation shifted to around −50 μm, meaning that the wall thickness is smaller than for samples with contour. This is also supported by the wall thickness analysis shown in Fig. 6b and visualized in Fig. 5. The mean wall thickness for samples with contour was 0.28 ± 0.05 mm and for samples without contour 0.20 ± 0.06 mm. The wall thickness distribution of the CAD design is also presented on the plot, and it lies closer to the wall thickness of the structures produced with contour. The relative densities of the two structures were also determined to be 44% for the samples with contour scan and 30% for the samples without contour scan. The differences in geometry and relative density have to be taken into account when evaluating the mechanical performances.

This result could be expected from Fig. 2c, as the distance – also called offset – of the scan vectors of the *in-fill* region to the nominal part edges was unchanged. In future work, additional parts without contour could be produced by adjusting the offset of these scan vectors, to reduce the frequency of negative deviations seen in Fig. 6a. Despite this adjustment, the broad distribution of wall thicknesses depicted in Fig. 6b for samples without contour scanning would still be present.

3.3. Porosity and microstructure

Fig. 7 displays the XY cross-section of the lattices imaged by LOM. It highlights that small spherical pores are present within the nodes and walls of the gyroid structure for all conditions. For all lattices, an internal porosity of about 0.4% was obtained, while less than 0.1% was measured on the cross-section of the bulk reference cubes. The pore morphology suggests that these are gas porosities formed in the thin walls and nodes of the structures. The porosity distribution appears similar for the two gases. The presence of this porosity may be owing to the fact that standard parameters are optimized for bulk parts. It could be that in the thin features (walls and nodes), there is less re-heating/-melting of the deposited material and thus less porosity healing possible than in for example solid cubes.

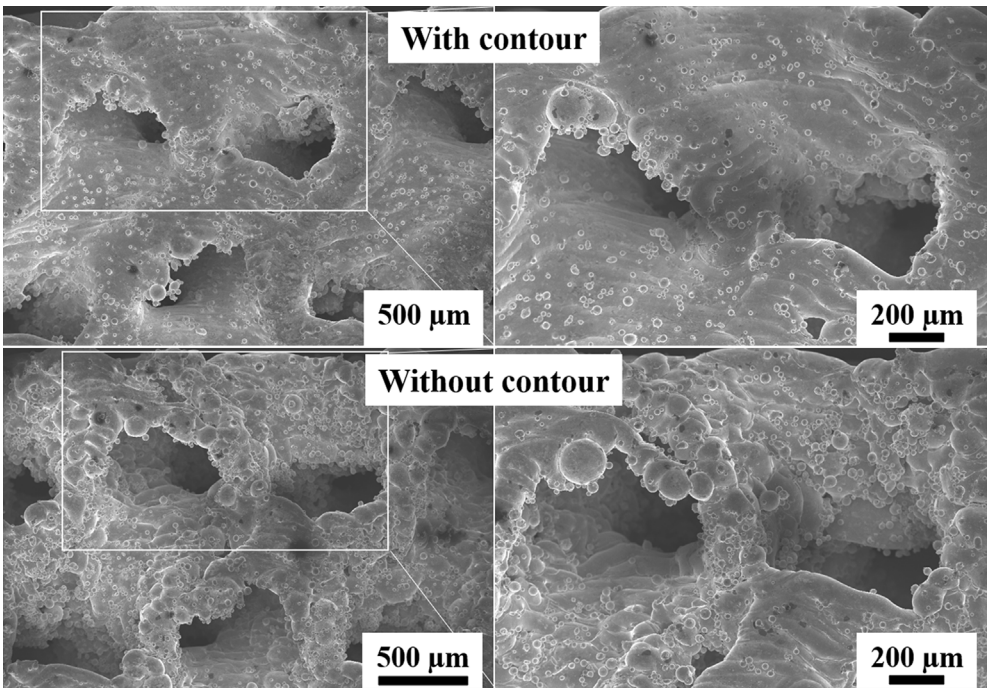

Fig. 4. Scanning electron micrographs of the front side of the lattices produced under Ar, with and without contour scanning.

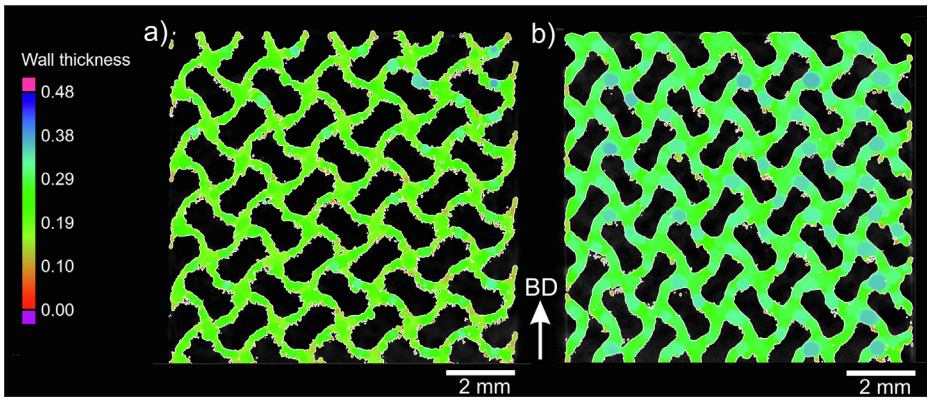

Fig. 5. XCT reconstructed slice along the building direction for lattices (a) without contour under Ar-He, (b) with contour under Ar-He. The colouring represents wall thickness distribution, see scale bar to the left.

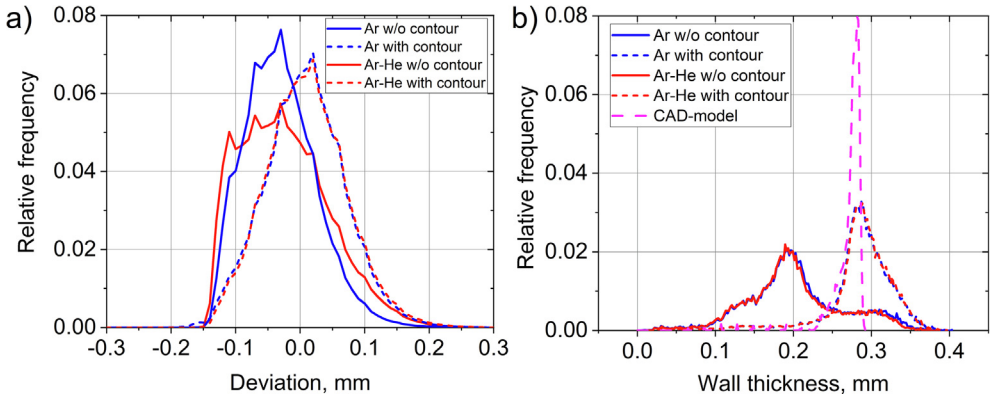

Fig. 6. (a) Deviations obtained by nominal-actual comparison (NAC) analysis, (b) wall thickness distribution.

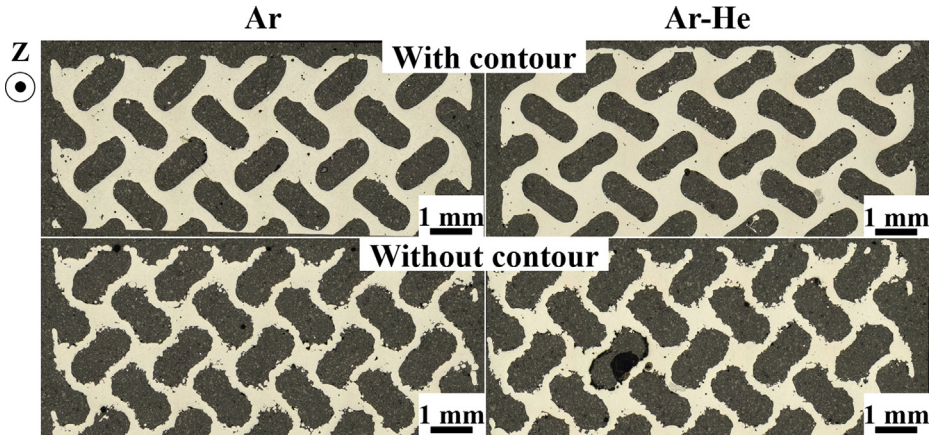

Fig. 7. Light optical micrographs of the XY cross-sections of the lattices built under Ar and Ar-He atmospheres with and without contour scan. Note: axis Z corresponds to the building direction.

Fig. 8 displays the EBSD orientation maps in the building direction of the XY cross-sections of the nodes of the lattice structures. It reveals that the nodes in the lattices built without contour mostly exhibit edges with partially melted or sintered powder particles, poorly bonded together, while the microstructure at the centre of the nodes exhibit larger grains recalling that of bulkier structures such as cubes. For comparison, similar maps are displayed for the XY cross-section of a standard cube in Fig. 9. Along the building direction, on the Z cross-section both the lattice structures and the standard dense cube exhibit grains slightly elongated in the Z direction. For the lattice, the down-skin is clearly characterized by the presence of sintered particles. Regardless of the process atmosphere, the orientation of the grains appears rather random as depicted by the IPF colouring.

3.4. Mechanical performance

Fig. 10 displays the stress–strain response under compressive loading of all tested specimens. The compressive stress measure is the engineering stress computed with a nominal cross-

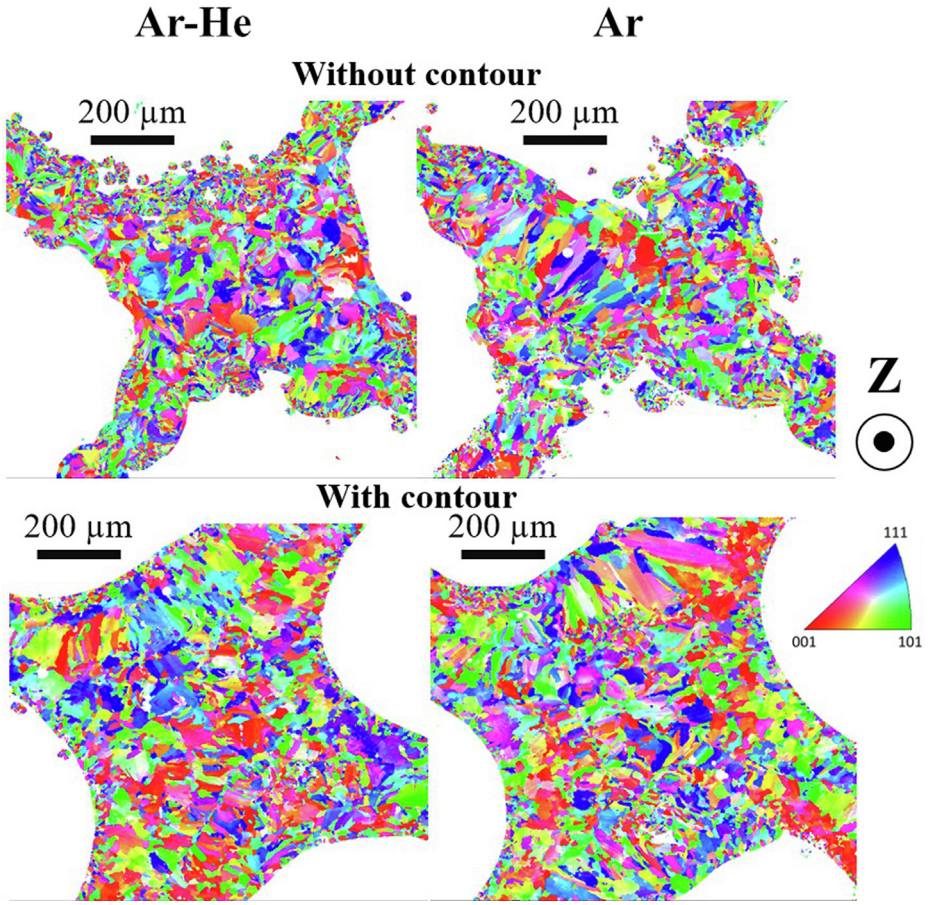

Fig. 8. EBSD orientation maps in the building direction of the nodes of the lattice structures on the XY cross-section, built under Ar-He and Ar, with and without contour scanning.

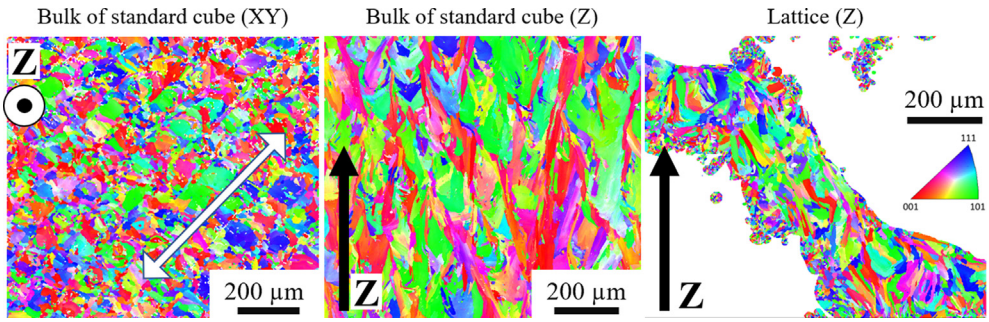

Fig. 9. EBSD orientation maps in the building direction of the bulk of a standard cube on the XY and Z cross-section, and of a lattice on the Z cross-section.

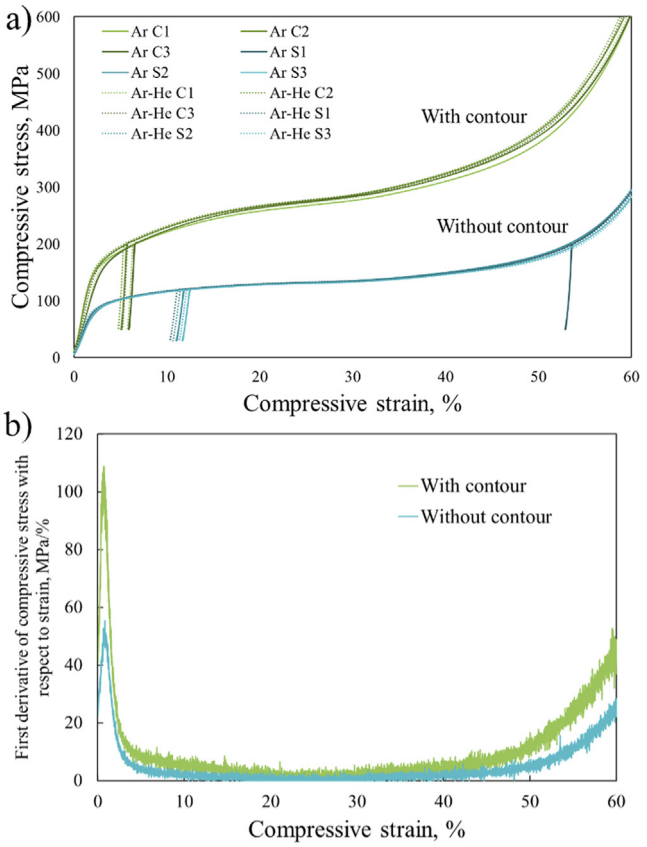

Fig. 10. (a) Compression curves of all the tested lattices. C stands for Contour and S for without contour; (b) First derivative of the stress as a function of strain.

sectional area of 100 mm^2. A clear difference in behaviour can be noted between the structures produced with and without contour scanning, while the effect of the atmosphere appears minor regarding the mechanical performance. Still, all samples do exhibit a three-stage deformation behaviour, with an initial stiff regime, followed by a long steady plateau region, and finally a rapid increase in stress corresponding to escalating densification of the compressed structure. As observed by Zhang et al. [3] and Liang et al. [4] for gyroid stainless steel structures produced by LPBF, a continuous and smooth hardening behaviour is recorded, without distinct peak stress and without the stress fluctuations often seen in other metallic cellular structures of similar relative densities. Such variations are typically caused by localised buckling of thin walls, collapse of entire layers or shearing of internal planes.

The lattices built with contour, with a higher relative density (44% dense) compared to the second type of samples (30% dense), exhibit both a higher elastic gradient (about 2.7 times) and a twice as high plateau stress, see Table 2. Fig. 10 suggests a more rapid densification of the structure built with contour from around 50% strain, which can be connected to the larger wall thickness resulting in earlier contact of the gyroid structure walls.

Babamiri et al. [23] compared the mechanical properties of Alloy 718 bulky samples, under compression and tension in as-built state. They measured a $\sigma_{0.2}$ of 618 MPa in compression and 524 MPa in tension. Following heat treatment, they obtained similar $\sigma_{0.2}$ in tension (1100 MPa) as that reported by the manufacturer of the machine used in the present work (1145 MPa [24]). As recalled by Maconachie et al. [25], the Gibson-Ashby model is widely used to predict the properties of cellular structures such as lattices. For structures exhibiting a steady plateau, and thus with a bending-dominated response, the following relationship between the strength of the bulk material and that of the lattice was proposed [26]:

$$\frac{\sigma_{lattice}}{\sigma_{bulk}} = C\left(\frac{\rho_{lattice}}{\rho_{bulk}}\right)^{\frac{3}{2}}$$

where $\sigma_{lattice}$ and σ_{bulk} are the strength of the lattice and corresponding bulk material respectively, $\rho_{lattice}/\rho_{bulk}$ is the relative density of the lattice (measured in this work by XCT), and C is the Gibson-Ashby constant which is empirical and depends on the unit cell topology and geometry. Based on the measured offset yield strength with and without contour (see Table 2) and the bulk compressive properties from [23], C is estimated to be 0.8 in the present work.

Thanks to the continuously increasing stress response during compression of the gyroid structures in this study, the potential for energy absorption is very high. The Alloy 718 lattice structures produced seem to counterfeit simple buckling of struts and thus invoke plastic deformation in a large part of the volume. It is expected that if the material would be used in a crash box or similar application, it would not collapse but continuously deform giving a more and more dense structure, with the energy absorbed proportional to the integrated area below the curve in Fig. 10a. The energy absorption for the structure built with contour scan is approximately twice as high although the relative density is less than 50% higher. The structure built with contour scan thus has the highest specific energy absorption.

The uneven deformation commonly seen in compression of less dense metallic cellular structures are typically caused by localised buckling of thin walls, and collapse of entire layers or shearing of internal planes, see for example [27,28]. In solid beams intended for energy absorption (crash beams, crash boxes), bending deformation rather than buckling has to be accomplished by geometrical notches or local thermal treatments. In the current rather dense gyroid structures, the function is built-in from the start. It should be highlighted that this gyroid design could be further optimised

Table 2
Properties of the gyroid lattices derived from the compression tests.

Condition	Average plateau stress, MPa	Average plateau end strain, %	Quasi-elastic gradient, GPa	Elastic gradient, GPa	0.2% offset yield strength ($\sigma_{0.2}$), MPa
Ar with contour	272.5 ± 4.5	46.2 ± 0.5	7.6 ± 1.6	26.5 ± 1.1	141.51 ± 5.9
Ar-He with contour	275.0 ± 2.5	46.1 ± 0.1	7.2 ± 1.5	27.9 ± 0.5	143.1 ± 2.7
Ar without contour	131.8 ± 0.9	48.7 ± 0.5	4.2 ± 0.3	12.3 ± 0.2	81.3 ± 9.8
Ar-He without contour	131.9 ± 1.1	49.1 ± 0.5	5.2 ± 0.3	12.4 ± 0.1	77.5 ± 1.7

for energy absorption applications by reducing its relative density (here nominal value 0.41) while keeping a minimum wall thickness, to achieve higher densification strain, still with a constant plateau region.

4. Discussions

The collection of the emissions in the near-IR range for each printed layer with the EOSTATE Exposure OT system highlights that Alloy 718 spatters emitting light in these wavelengths cool faster with addition of He and are reduced in amount. These findings are in good agreement with the reduction of incandescent Ti-6Al-4V spatters with He investigated by means of shadowgraphy [29]. It was shown that such generations were reduced by 60% in pure He and that their cooling rates were approximately twice those observed in pure Ar. Similar amount of Alloy 718 spatters were collected in the present work at the gas inlet and outlet. It could be that the build volume utilisation is too little to generate significant differences in that respect. While evidence of faster particle cooling with He were collected, the microstructural investigations of the produced gyroid structures highlight very similar solidification structure regardless of the process atmosphere. Indeed, similar grain morphology and orientation were derived from the EBSD evaluation, and cell sizes observed by SEM remained comparable. This correlates well to the previous work conducted on 316L stainless steel processed under Ar, N_2 and He [30], where the generally reported ⟨101⟩ preferential orientation in the building direction was obtained regardless of the process gas. The effect of He on the spatter cooling was previously discussed in [29], by comparing the particle-to-gas convection in Ar and He considering the heat transfer coefficient (h) upon cooling of a particle under each gas. It was shown that h_{He} prevails significantly over h_{Ar}. When considering the deposited material and the melt pool, it is expected that the observed reduction of spatter generation is associated with a more continuous energy input and stable melt flow. Still, the heat transfer during melt pool cooling is dominated by heat conduction to the layers below; the impact of gas convection is small as compared to the case of a particle surrounded by gas. Radiation of heat is more efficient during the flight of the particle. This is the proposed explanation to the differences observed in terms of spatters but not of deposited material.

Another important reduction of recorded spatter signal was observed when the laser contour scanning was not applied as noted from Fig. 3. For each gas, the reduction observed for structures without contour is solely attributed to a decrease in spatter amount and not their cooling rate because of the increased scanned area of the part by laser. This total scanned area for each printed part may have important consequences for the total time required to scan each layer. Therefore, it is of interest to consider the contribution of contour scanning to the overall build duration and its effect on productivity. For simple and dense geometries with few surfaces such as cubes, contour scanning takes up a very small part of the overall laser path. However, for lattices of high specific surface area, the contour becomes more dominant. The build preparation software *EOSPrint 2.8* provided by the machine manufacturer allows to estimate the build time for a defined print job, considering both recoating and exposure time contributions. Table 3 lists the computed duration for different build job configurations presented in Fig. 11. The recoating time is calculated from the number of layers and the recoating speed (here 80 mm/s). Hence, for all the configurations with constant lattice height the recoating time is constant and equal to 1 h 30 min. For comparison, similar calculations were conducted for more conventional and bulky part design: rings with 25 mm internal diameter, 80 mm outer diameter and 48 mm height (resulting in about 4 times more layers than the lattices), see Fig. 11. From the results presented in Table 3, it is evident that the contribution of contour scanning to total build time are only relevant to components with a large surface area per unit volume. Also, judging from the density measurements made in this study, the contour scan added more material, and gave much better agreement with the nominal CAD geometry. In essence, the build time comparison would be even more beneficial for contour scan, using modified CAD geometries yielding the same final net shape and density.

Addition of He to the process gas and printing without contour scanning both lead to a reduction of the generation of spatter. However, only the removal of the contour scanning has a very determining effect on the final gyroid dimension as compared to the input design, see Figs. 6–8. Overall, the absolute deviation obtained by NAC analysis increased when contour scanning was not applied, and the wall thickness decreased. This effect is held responsible for the impaired compressive properties recorded, see Fig. 10. In addition, as discussed by Catchpole-Smith et al. [31], the sintered particles on the inner walls of the lattices printed without contour as seen in Fig. 8, will have reduced thermal transport ability because of the poor metallurgical and physical bond to the structure. This aspect should be kept in mind when designing components such as heat exchangers.

To further compare the deformation behaviour of the lattices produced with and without contour scanning, intermediate compression tests were performed up to intermediate strain levels, as displayed in Fig. 12. The strain levels were selected to be at the beginning and towards the end of the steady plateau regime, see Fig. 10. The pre-strained samples were then evaluated by XCT following an identical procedure as for the unstrained specimens, see Figs. 13 and 14. Both sections displaying the vertical and horizontal

Table 3
Build job duration computed using EOSPrint 2.8 for different configurations. In parenthesis, the reduction in duration is given taking the equivalent configuration with contour settings as reference.

Build job configuration	Total build time
1 lattice with contour	1 h 46 min
1 lattice without contour	1 h 42 min (−3.8%)
20 lattices with contour	7 h 00 min
10 lattices with contour + 10 without contour	6 h 20 min (−9.5%)
196 lattices with contour	55 h 25 min
196 lattices without contour	40 h 23 min (−27%)
4 large rings with contour	138 h 20 min
4 large rings without contour	136 h 28 min (−2%)

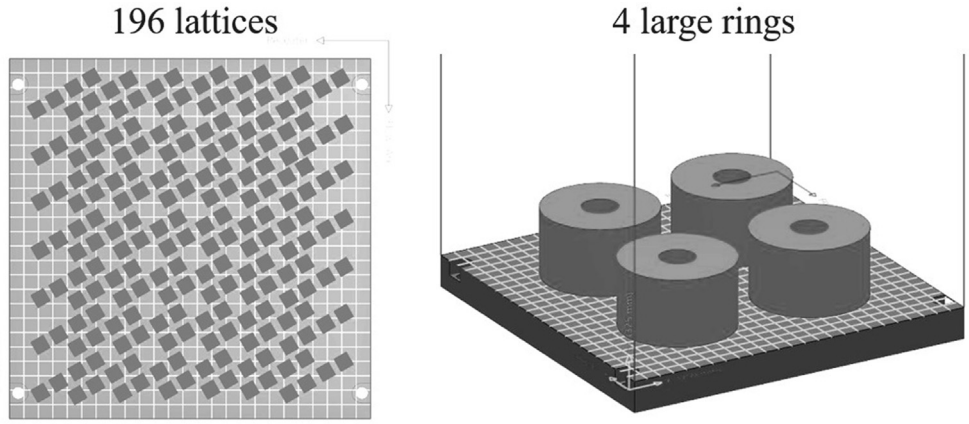

Fig. 11. Considered build job configurations for the analysis of productivity and effect of contour scanning with 196 gyroid lattices and 4 large rings.

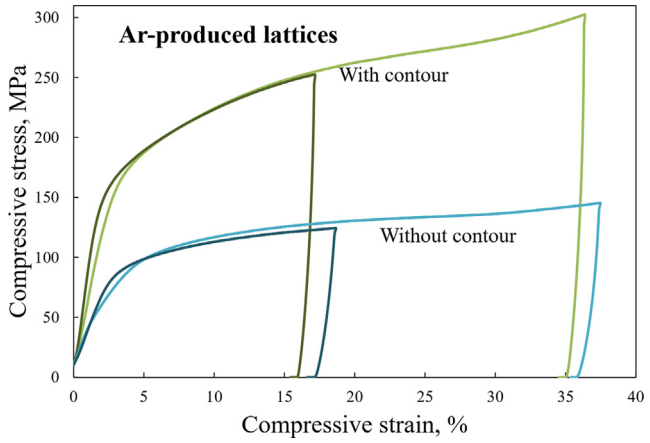

Fig. 12. Compression curves of Ar-produced lattices up to intermediate strain levels.

walls of the gyroid structures are presented. As mentioned above, the gyroid structure seems to utilize the material in a favourable way, inducing bending and compressive deformation rather than buckling of struts. The Euler buckling resistance (critical load of elastic buckling) of individual struts would with some approximation be proportional to the thickness of the struts raised to the power of 4 based on the area moment of inertia. Using the measured average thicknesses, 0.20 mm without contour scan, and 0.28 mm with, the expected ratio between the critical buckling load would be 3.8. Since plastic deformation of the structure is invoked early, it might be more suitable to compare the beam bending resistance, which would rather be proportional to the thickness raised to the power of 3. This gives a scale factor around 2.7 which is closer to the observed relation in stress responses (2.0). A plausible explanation to this difference is that only parts of the structure are activated for plastic deformation.

It is evident from the XCT that in both structures little internal contacts occur before 16% strain, but at 35% remaining strain there is densification in the inner parts of the samples, stronger in the samples with contour scan. The complicated gyroid geometry is

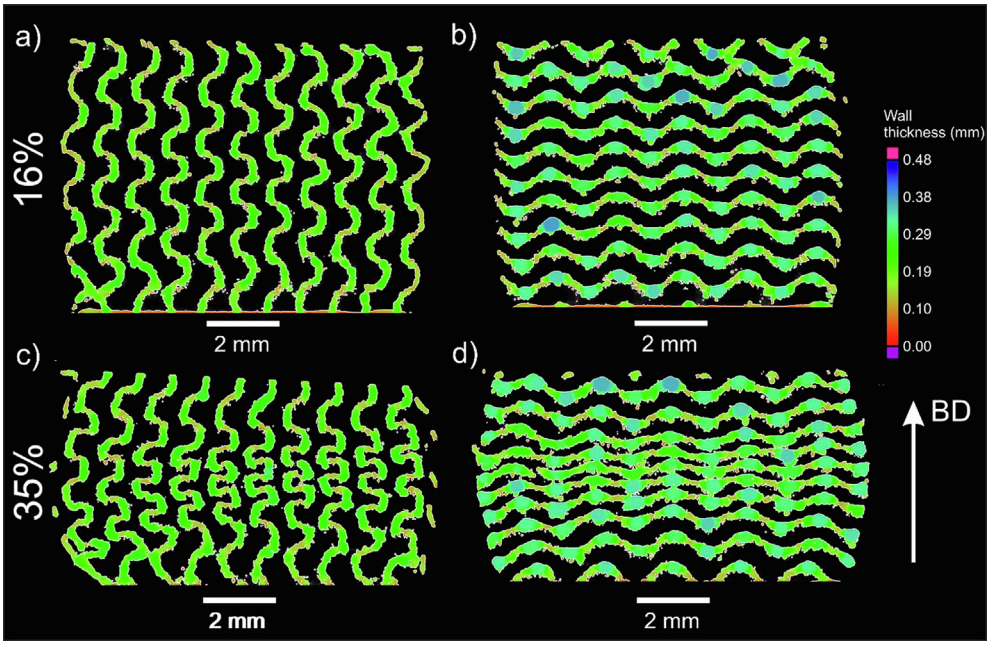

Fig. 13. XCT reconstructed cross sections of the pre-strained sample without contour produced in Ar for: (a) vertical walls ~16% pre-strained, (b) horizontal walls ~16% pre-strain; and (c) vertical walls ~35% pre-strained, (d) horizontal walls ~35% pre-strain.

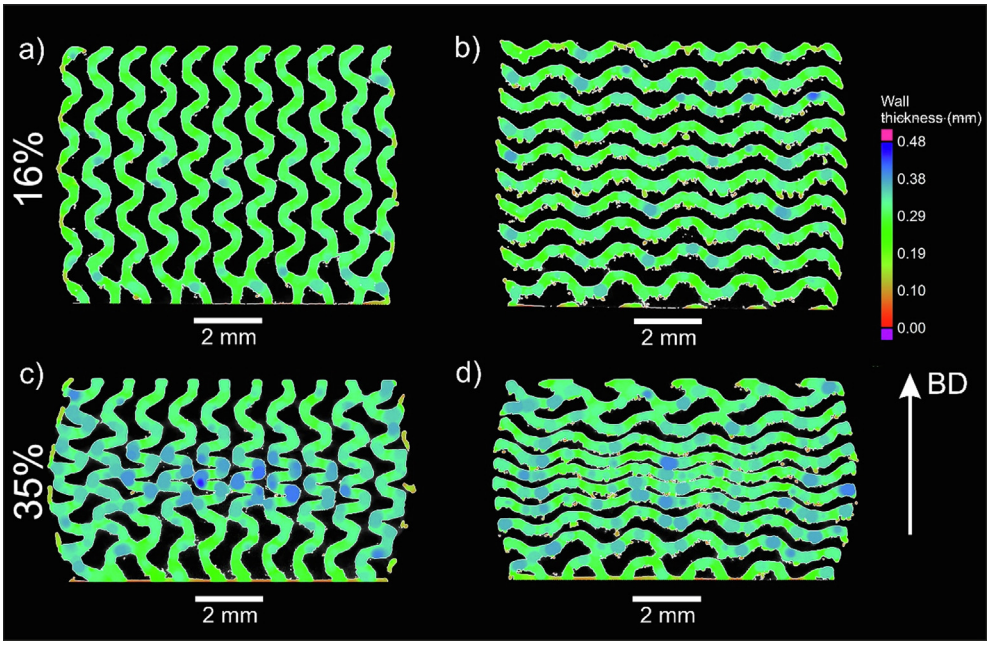

Fig. 14. XCT reconstructed cross sections of the pre-strained sample with contour for: (a) vertical walls ~16% pre-strained, (b) horizontal walls ~16% pre-strain; and (c) vertical walls ~35% pre-strained, (d) horizontal walls ~35% pre-strain.

of course not directly comparable to pure buckling or bending of straight beams, and further modelling using Finite element analysis would be necessary for precise evaluation of the deformation modes. A challenge is the contact simulation, when internal contact occurs and start transferring significant portions of the force.

5. Conclusions

Contour scanning appears necessary to ensure high geometrical accuracy of complex components produced by laser powder bed fusion. The nominal strength of as-built Alloy 718 lattices was shown to increase with the scanning of contours ($\sigma_{0.2} \sim 140$ MPa with contour and ~80 MPa without), partly because of the higher relative density (0.44 compared to 0.33). Still, even without contour scanning, the produced lattices exhibit a continuously increasing stress response under compression, very desirable for energy absorption applications. XCT of the as-built and compression-strained lattices highlighted that these gyroid structures utilize the material in a favourable way showing bending and compression deformation without strut buckling. This is also depicted in the stress–strain curve; densification appearing earlier for the lattices built with contour, yields stronger hardening. Similar responses under compression and similar microstructures of the as-built lattices were obtained for the two process gases used (Ar and a mixture of Ar-He). This suggests that the higher thermal conductivity of the process gas did not significantly impact the cooling rate and solidification of the deposited Alloy 718 material. Still, an important reduction in spatter temperature and quantity with Ar-He mixture was registered using the monitoring system of the printer which collects radiation from the baseplate in the near-infrared range. This is particularly promising to increase process stability and limit powder bed degradation, enhance powder reusability and the process sustainability.

Data availability

The data that support the findings of this study are available from the corresponding author upon reasonable request.

Declaration of Competing Interest

The authors declare that they have no known competing financial interests or personal relationships that could have appeared to influence the work reported in this paper.

Acknowledgements

This work was conducted in the framework of the Centre for Additive Manufacturing – Metal (CAM^2), supported by the Swedish Governmental Agency of Innovation Systems (Vinnova). Additional acknowledgements are addressed to Bo Williamsson, Linde Gas AB, for his help with the gas mixture installation at Chalmers University of Technology.

References

[1] ASTM International, ISO/ASTM 52900: Standard Terminology for Additive Manufacturing – General Principles – Terminology, ASTM Int. I (2015) 1–9. http://compass.astm.org/EDIT/html_annot.cgi?ISOASTM52900+15.
[2] L.J. Gibson, Cellular Solids, MRS Bull. 28 (4) (2003) 270–274.
[3] L. Zhang, S. Feih, S. Daynes, S. Chang, M.Y. Wang, J. Wei, W.F. Lu, Energy absorption characteristics of metallic triply periodic minimal surface sheet structures under compressive loading, Addit. Manuf. 23 (2018) 505–515, https://doi.org/10.1016/j.addma.2018.08.007.
[4] Y. Liang, W. Zhou, Y. Liu, Z. Li, Y. Yang, H. Xi, Z. Wu, Energy Absorption and Deformation Behavior of 3D Printed Triply Periodic Minimal Surface Stainless Steel Cellular Structures under Compression, Steel Res. Int. 92 (3) (2021) 2000411, https://doi.org/10.1002/srin.202000411.
[5] C. Yan, L. Hao, A. Hussein, P. Young, D. Raymont, Advanced lightweight 316L stainless steel cellular lattice structures fabricated via selective laser melting, Mater. Des. 55 (2014) 533–541, https://doi.org/10.1016/j.matdes.2013.10.027.
[6] R.C. Reed, The Superalloys: Fundamentals and Applications, Cambridge University Press, 2009.
[7] S. Parbat, Z. Min, L. Yang, M. Chyu, Experimental and numerical analysis of additively manufactured inconel 718 coupons with lattice structure, J. Turbomach. 142 (2020) 1–9, https://doi.org/10.1115/1.4046527.
[8] N. Korshunova, G. Alaimo, S.B. Hosseini, M. Carraturo, A. Reali, J. Niiranen, F. Auricchio, E. Rank, S. Kollmannsberger, Image-based numerical characterization and experimental validation of tensile behavior of octet-truss lattice structures, Addit. Manuf. 41 (2021) 101949, https://doi.org/10.1016/j.addma.2021.101949.
[9] Z.S. Bagheri, D. Melancon, L. Liu, R.B. Johnston, D. Pasini, Compensation strategy to reduce geometry and mechanics mismatches in porous

biomaterials built with Selective Laser Melting, J. Mech. Behav. Biomed. Mater. 70 (2017) 17–27, https://doi.org/10.1016/j.jmbbm.2016.04.041.
[10] M. Dallago, B. Winiarski, F. Zanini, S. Carmignato, M. Benedetti, On the effect of geometrical imperfections and defects on the fatigue strength of cellular lattice structures additively manufactured via Selective Laser Melting, Int. J. Fatigue. 124 (2019) 348–360, https://doi.org/10.1016/j.ijfatigue.2019.03.019.
[11] K. Artzt, T. Mishurova, P. Bauer, J. Gussone, P. Barriobero-vila, S. Evsevleev, G. Bruno, G. Requena, J. Haubrich, Pandora's Box – Influence of Contour Parameters on Roughness and Subsurface Residual Stresses in Laser Powder Bed Fusion of Ti-6Al-4V, Mater. MDP I (2020) 1–24, https://doi.org/10.3390/ma13153348.
[12] A. Leicht, M. Rashidi, U. Klement, E. Hryha, Effect of process parameters on the microstructure, tensile strength and productivity of 316L parts produced by laser powder bed fusion, Mater. Charact. 159 (2020) 110016, https://doi.org/10.1016/j.matchar.2019.110016.
[13] C. Pauzon, P. Forêt, E. Hryha, T. Arunprasad, Effect of Helium – Argon Mixtures as Laser – Powder Bed Fusion Processing Atmospheres on the Properties of the Built Ti-6Al-4V Parts, in: WorldPM2018, WorldPM 2018 Bejijng, 2018, pp. 1633–1639.
[14] S. Traore, M. Schneider, I. Koutiri, F. Coste, R. Fabbro, C. Charpentier, P. Lefebvre, P. Peyre, Influence of gas atmosphere (Ar or He) on the laser powder bed fusion of a Ni-based alloy, J. Mater. Process. Tech. 288 (2021) 116851, https://doi.org/10.1016/j.jmatprotec.2020.116851.
[15] C. Pauzon, Tailored process gases for laser powder bed fusion, 2021. https://research.chalmers.se/en/publication/522522%0Ahttps://research.chalmers.se/publication/522522/file/522522_Fulltext.pdf.
[16] C. Pauzon, A. Raza, E. Hryha, P. Forêt, Oxygen balance during laser powder bed fusion of Alloy 718, Mater. Des. 201 (2021) 109511, https://doi.org/10.1016/j.matdes.2021.109511.
[17] A.H. Schoen, Infinite periodic minimal surfaces without self-intersections, Nasa Tech. Note D-5541. (1970) 92. http://ntrs.nasa.gov/search.jsp?R=19700020472.
[18] C. Pauzon, E. Hryha, P. Forêt, L. Nyborg, Effect of argon and nitrogen atmospheres on the properties of stainless steel 316 L parts produced by laser-powder bed fusion, Mater. Des. 179 (2019) 107873, https://doi.org/10.1016/j.matdes.2019.107873.
[19] ImageJ: Image Processing and Analysis in Java, (n.d.). https://imagej.nih.gov/ij/index.html (accessed March 2, 2020).
[20] M. Fischer, S. Dubiez - Le Goff, D. Campion, G. Volpi, Submitted for journal publication/Unpublished results: A method for melt pool stability and spatter analysis during laser powder bed fusion process using industrial monitoring systems, (2021).
[21] International Organization for Standardization, Mechanical testing of metals – Ductility testing – Compression test for porous and cellular metals (ISO Standard No. 13314:2011(E)), Int. Organ. Stand. 2011 (2011) 1–7. www.iso.org.
[22] L. Bjerregaard, K. Geels, B. Ottesen, M. Rückert, Metalog Guide (2002).
[23] B.B. Babamiri, J. Indeck, G. Demeneghi, J. Cuadra, K. Hazeli, Quantification of porosity and microstructure and their effect on quasi-static and dynamic behavior of additively manufactured Inconel 718, Addit. Manuf. 34 (2020) 101380, https://doi.org/10.1016/j.addma.2020.101380.
[24] E. GmbH, Electro Optical Systems, EOS NickelAlloy IN718 Material Data Sheet 49 (2020) 5.
[25] T. Maconachie, M. Leary, B. Lozanovski, X. Zhang, M.a. Qian, O. Faruque, M. Brandt, SLM lattice structures: Properties, performance, applications and challenges, Mater. Des. 183 (2019) 108137, https://doi.org/10.1016/j.matdes.2019.108137.
[26] M.F. Ashby, The properties of foams and lattices, Phil. Trans. R. Soc. A 364 (1838) (2006) 15–30.
[27] H. Lei, C. Li, J. Meng, H. Zhou, Y. Liu, X. Zhang, P. Wang, D. Fang, Evaluation of compressive properties of SLM-fabricated multi-layer lattice structures by experimental test and μ-CT-based finite element analysis, Mater. Des. 169 (2019) 107685, https://doi.org/10.1016/j.matdes.2019.107685.
[28] D. Khrapov, M. Kozadayeva, K. Manabaev, A. Panin, W. Sjöström, A. Koptyug, T. Mishurova, S. Evsevleev, D. Meinel, G. Bruno, D. Cheneler, R. Surmenev, M. Surmeneva, Different approaches for manufacturing ti-6al-4v alloy with triply periodic minimal surface sheet-based structures by electron beam melting, Materials (Basel) 14 (17) (2021) 4912, https://doi.org/10.3390/ma14174912.
[29] C. Pauzon, B. Hoppe, T. Pichler, S. Dubiez-Le Goff, P. Forêt, T. Nguyen, E. Hryha, Reduction of incandescent spatter with helium addition to the process gas during laser powder bed fusion of Ti-6Al-4V, CIRP J. Manuf. Sci. Technol. 35 (2021) 371–378, https://doi.org/10.1016/j.cirpj.2021.07.004.
[30] C. Pauzon, A. Leicht, U. Klement, P. Forêt, E. Hryha, Effect of the process gas and scan speed on the properties and productivity of thin 316L structures produced by laser-powder bed fusion, Metall. Mater. Trans. A 51 (10) (2020) 5339–5350, https://doi.org/10.1007/s11661-020-05923-w.
[31] S. Catchpole-Smith, R.R.J. Sélo, A.W. Davis, I.A. Ashcroft, C.J. Tuck, A. Clare, Thermal conductivity of TPMS lattice structures manufactured via laser powder bed fusion, Addit. Manuf. 30 (2019) 100846, https://doi.org/10.1016/j.addma.2019.100846.